Mixed Potential Integral Equation Technique for Hybrid Microstrip-Slotline Multilayered Circuits Using a Mixed Rectangular-Triangular Mesh

Jeannick Sercu, *Student Member, IEEE,* Niels Faché, *Member, IEEE,*
Frank Libbrecht, and Paul Lagasse, *Senior Member, IEEE*

***Abstract*—In this paper, a mixed potential integral equation (MPIE) formulation for hybrid microstrip-slotline multilayered circuits is presented. This integral equation is solved with the method of moments (MoM) in combination with Galerkin's method. The vector-valued rooftop functions defined over a mixed rectangular-triangular mesh are used to model the electric and magnetic currents on the microstrip and slotline structures. An efficient calculation technique for the quadruple interaction integrals between two cells in the system matrix equation is presented. Two examples of hybrid microstrip-slotline circuits are discussed. The first example compares the simulation results for a microstrip-slotline transition with measured data. The second example illustrates the use of the simulation technique in the design process of a broadband slot-coupled microstrip line transition.**

I. Introduction

THE METHOD of moments (MoM) has been widely used for the analysis of general 3D structures [1] and predominantly planar microstrip and slotline structures [2]–[16]. Several commercial MoM software packages for the analysis of microstrip and slotline circuits have emerged in recent years [17]–[21]. Most of them have the restriction that a uniform rectangular mesh is used. This implies that the designer must carefully consider what cell size to use in order to best approximate the geometry of interest with the resulting metallization mesh.

Flexible meshes consisting of different types of rectangular and/or triangular cells overcome the geometrical limitations of a uniform mesh. Recently, some research groups have started to investigate the use of triangular meshes and mixed meshes of rectangles and triangles. Chang and Zheng [10] have developed the P-mesh algorithm. This algorithm is derived from the application of the MoM to a spatial domain mixed potential integral equation governing the behavior of a microstrip circuit. Rectangular cells are used in the transmission lines of the microstrip circuit, while triangular cells are used to represent the microstrip discontinuities. The expansion and test functions are the classical vector-valued rooftop functions with rectangular or triangular support. Horng *et al.* [11] have investigated the compensation of microstrip discontinuities using vector-valued triangular subdomain functions as both expansion and testing functions in the MoM. In [11], the electric field integral equation is solved in the spectral domain. A mesh consists of one or more different types of triangles.

In this paper, a new research contribution to the application of mixed meshes in the MoM modelling of planar circuits is presented. The mixed potential integral equation (MPIE) formulation is extended to govern the electromagnetic behavior of hybrid microstrip-slotline multilayered circuits. Magnetic surface currents are introduced at the slotline structures to represent the tangential electric field in the slotline apertures. A mixed mesh of rectangular and triangular cells is used to model the electric and magnetic currents on the microstrip and slotline structures. The Green's function kernels can be represented by classical Sommerfeld-type integrals. For these integrals accurate and efficient numerical integration schemes exist [22], [23].

The MPIE formulation has been favored over the electric and magnetic field integral equation formulation [14], [15]. In comparison with the components of the electric field Green's dyadic, the Green's functions in the MPIE formulation are less singular, i.e. they only exhibit a $1/\rho$ singularity instead of the $1/\rho^3$ singularity in [14] ($\rho = |\boldsymbol{r} - \boldsymbol{r}'|$ represents the lateral distance between an observation point $\boldsymbol{r}$ and an excitation point $\boldsymbol{r}'$). This makes the evaluation of the interactions between two cells more simple and stable. Moreover, unlike the EFIE Green's dyadic components the MPIE Green's functions do not depend on the direction of the vector which connects the excitation and observation point, i.e. the MPIE Green's functions are one-dimensional functions of ρ. Our algorithm makes use of this property.

The MPIE is solved in the spatial domain using the method of moments. A spatial domain approach makes it possible to perform the computationally expensive calculation of the Green's functions once and store the data for future simulations of circuits printed on the same substrate. A mesh maker has been developed to mesh any planar circuit of arbitrary polygonal shape in triangles and rectangles. Using this mesh the unknown electric and magnetic current density can be expanded into rooftop functions. The application of the Galerkin MoM reduces the computational burden to the calculation of the spatial interaction integrals between two cells in the interaction matrix equation $\boldsymbol{Z} \cdot \boldsymbol{I} = \boldsymbol{V}$ and to the solution of this matrix equation. This solution provides the amplitudes of the current expansion functions.

Manuscript received December 16, 1993; revised August 26, 1994.

The authors are with the Laboratory of Electromagnetism and Acoustics (LEA), University of Ghent, 9000 Ghent, Belgium.

IEEE Log Number 9410342.

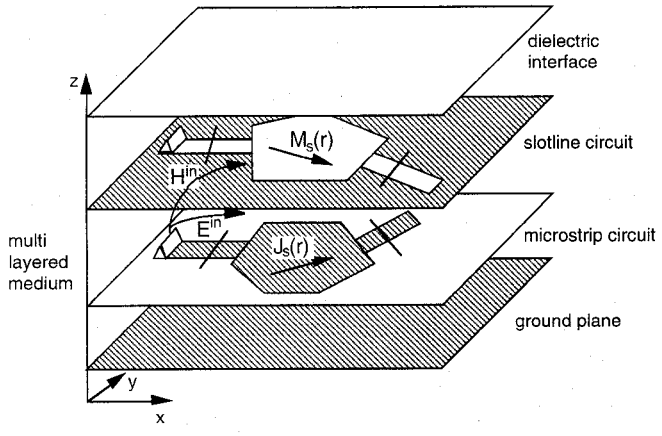

Fig. 1. Picture of a general microstrip-slotline planar structure embedded in a multilayered medium.

An analytical calculation technique for the quadruple interaction integrals between two cells in the system matrix equation $\boldsymbol{Z} \cdot \boldsymbol{I} = \boldsymbol{V}$ is discussed in Section III. For each interaction integral the Green's functions are approximated using a local power series expansion of ρ. The number of expansion terms depends on the distance between the cells. With each power term a quadruple power-moment integral is associated. An analytical technique has been developed for the calculation of these quadruple integrals. Recurrence relations make the calculations very efficient. For distant coupling a Taylor's series approximation of the powers of ρ is used to speed up the calculations significantly.

The last section of the paper presents some numerical simulation results for two practical hybrid microstrip-slotline structures. The first example shows the simulation results for a microstrip-slotline transition. These results are compared with theoretical and measured data found in the literature. The second example illustrates the use of the simulation technique in the design proces of a broadband slot-coupled microstrip line transition with a maximally flat transmission characteristic in the X-band.

II. Mixed Potential Integral Equation Formulation for Hybrid Microstrip-Slotline Structures

The geometry of a general hybrid microstrip-slotline structure embedded in a multilayered medium is depicted in Fig. 1. A microstrip circuit S_m consists of a finite metallization pattern at a dielectric interface, while a slotline circuit S_s consists of a finite aperture in a infinite metallization pattern. The tangential electric field at the slotline circuits is represented by an equivalent magnetic surface current density $\boldsymbol{M}_s(\boldsymbol{r}) = \boldsymbol{u}_z \times \boldsymbol{E}(\boldsymbol{r})$. The vector $\boldsymbol{u}_z$ is the unit vector normal to the planar structure. The introduction of an equivalent magnetic current in the slotline structures reduces the meshing of the infinite metallization patterns at the slotline levels to the meshing of the finite slotline apertures.

An incoming electromagnetic field $\boldsymbol{E}^{\text{in}}, \boldsymbol{H}^{\text{in}}$ induces electric surface currents $\boldsymbol{J}_s(\boldsymbol{r})$ at the microstrip structures S_m and magnetic surface currents $\boldsymbol{M}_s(\boldsymbol{r})$ at the slotline structures S_s. In terms of vector and scalar potentials, the electric and magnetic field due to these surface currents are given by [16]

$$\boldsymbol{E}(\boldsymbol{r}) = -j\omega \boldsymbol{A}(\boldsymbol{r}) - \nabla V^A(\boldsymbol{r}) - \frac{1}{\varepsilon_i} \nabla \times \boldsymbol{F}(\boldsymbol{r}) \tag{1}$$

$$\boldsymbol{H}(\boldsymbol{r}) = -j\omega \boldsymbol{F}(\boldsymbol{r}) - \nabla V^F(\boldsymbol{r}) + \frac{1}{\mu_i} \nabla \times \boldsymbol{A}(\boldsymbol{r}) \tag{2}$$

where

$$\boldsymbol{A}(\boldsymbol{r}) = \iint_{S_m} \overline{\overline{\boldsymbol{G}}}^A(\boldsymbol{r}, \boldsymbol{r}') \cdot \boldsymbol{J}_s(\boldsymbol{r}')\, dS' \tag{3}$$

$$\boldsymbol{F}(\boldsymbol{r}) = \iint_{S_s} \overline{\overline{\boldsymbol{G}}}^F(\boldsymbol{r}, \boldsymbol{r}') \cdot \boldsymbol{M}_s(\boldsymbol{r}')\, dS' \tag{4}$$

and

$$V^A(\boldsymbol{r}) = -\frac{1}{j\omega} \iint_{S_m} G^{V_A}(\boldsymbol{r}, \boldsymbol{r}') \nabla \cdot \boldsymbol{J}_s(\boldsymbol{r})\, dS' \tag{5}$$

$$V^F(\boldsymbol{r}) = -\frac{1}{j\omega} \iint_{S_s} G^{V_F}(\boldsymbol{r}, \boldsymbol{r}') \nabla \cdot \boldsymbol{M}_s(\boldsymbol{r}')\, dS' \tag{6}$$

$\overline{\overline{\boldsymbol{G}}}^A(\boldsymbol{r}, \boldsymbol{r}')$ and $\overline{\overline{\boldsymbol{G}}}^F(\boldsymbol{r}, \boldsymbol{r}')$ are the Green's dyadics for the magnetic and electric vector potentials $\boldsymbol{A}(\boldsymbol{r})$ and $\boldsymbol{F}(\boldsymbol{r})$ in the layered medium and $G^{V_A}(\boldsymbol{r}, \boldsymbol{r}')$ and $G^{V_F}(\boldsymbol{r}, \boldsymbol{r}')$ are the corresponding scalar Green's functions for the electric and magnetic scalar potentials. The scalar potentials $V^A(\boldsymbol{r})$ and $V^F(\boldsymbol{r})$ are related with the vector potentials $\boldsymbol{A}(\boldsymbol{r})$ and $\boldsymbol{F}(\boldsymbol{r})$ by the Lorentz gauge [16].

For the description of the horizontal fields in a multilayered medium, the Sommerfeld potentials are very suitable [16]. With this type of potentials, the dyadic Green's functions for the magnetic and electric vector potentials are of the form

$$\begin{aligned}\overline{\overline{\boldsymbol{G}}}^A(\boldsymbol{r}, \boldsymbol{r}') = {} & \overline{\overline{\boldsymbol{I}}}_t G^A_{tt}(\rho, z, z') + \boldsymbol{u}_z \nabla'_t G^A_{zt}(\rho, z, z') \\ & + \boldsymbol{u}_z G^A_{zz}(\rho, z, z') \boldsymbol{u}_z \end{aligned} \tag{7}$$

$$\begin{aligned}\overline{\overline{\boldsymbol{G}}}^F(\boldsymbol{r}, \boldsymbol{r}') = {} & \overline{\overline{\boldsymbol{I}}}_t G^F_{tt}(\rho, z, z') + \boldsymbol{u}_z \nabla'_t G^F_{zt}(\rho, z, z') \\ & + \boldsymbol{u}_z G^F_{zz}(\rho, z, z') \boldsymbol{u}_z \end{aligned} \tag{8}$$

where $\overline{\overline{\boldsymbol{I}}}_t = \boldsymbol{u}_x \boldsymbol{u}_y + \boldsymbol{u}_y \boldsymbol{u}_y$ is the tangential unit dyadic and $\rho = \sqrt{(x-x')^2 + (y-y')^2}$ is the horizontal distance between the source and the field point. Only three scalar potential functions are needed to represent the nine components of the Green's dyadic for the vector potentials in a layered medium.

The mixed-potential integral equation formulation for hybrid microstrip-slotline circuits follows from the boundary conditions of the tangential electric field at the microstrip surface S_m and the tangential magnetic field at the surface S_s of the slotline apertures. Starting from the Sommerfeld forms (7) and (8) for the vector potentials in the layered medium, we can derive the following integral equations in the unknown surface currents:

$$\begin{aligned} & \iint_{S_m} dS' [G^A_{mm}(\rho, z_m, z'_m) \boldsymbol{J}_s(\boldsymbol{r}') \\ & \quad - \nabla (G^V_{mm}(\rho, z_m, z'_m) \nabla' \cdot \boldsymbol{J}_s(\boldsymbol{r}'))] \\ & \quad + \iint_{S_s} dS' [G^A_{ms}(\rho, z_m, z'_s)(\boldsymbol{u}_z \times \boldsymbol{M}_s(\boldsymbol{r}')) \\ & \quad - \nabla (G^V_{ms}(\rho, z_m, z'_s) \nabla' \cdot (\boldsymbol{u}_z \times \boldsymbol{M}_s(\boldsymbol{r}')))] \\ & = -\boldsymbol{E}^{\text{in}}(\boldsymbol{r}); \qquad \boldsymbol{r} \in S_m \end{aligned} \tag{9}$$

$$\iint_{S_s} dS'[G^A_{ss}(\rho, z_s, z'_s)\boldsymbol{M}_s(\boldsymbol{r}') - \nabla(G^V_{ss}(\rho, z_s, z'_s)\nabla' \cdot \boldsymbol{M}_s(\boldsymbol{r}'))] - \boldsymbol{u}_z \times \iint_{S_m} dS'[G^A_{sm}(\rho, z_s, z'_m)\boldsymbol{J}_s(\boldsymbol{r}') - \nabla(G^V_{sm}(\rho, z_s, z'_m)\nabla' \cdot \boldsymbol{J}_s(\boldsymbol{r}'))] = -\Delta\boldsymbol{H}^{\text{in}}(\boldsymbol{r}); \qquad \boldsymbol{r} \in S_s. \tag{10}$$

The derivation of (9) and (10) from (1)–(8) requires some analytical calculus, however this derivation is purely mathematically and straightforward and is therefore omitted here.

The first integral (9) follows from the electric field boundary condition at the microstrip circuit $z = z_m$. The left hand side of this equation has two contributions. The first contribution describes the tangential electric field excited by the electric surface currents at the microstrip circuit $z = z'_m$. This contribution is identical to the classical MPIE formulation for microstrip circuits [10]. The second contribution describes the tangential electric field excited by the equivalent magnetic surface current at the slotline circuit $z = z'_s$. The orientation of the magnetic current is rotated over 90° in the horizontal plane as a consequence of the rotor operator which acts on the electric vector potential $\boldsymbol{F}(\boldsymbol{r})$ in (1). The second integral (10) follows from the magnetic field boundary condition at the slotline circuits S_s. The right hand sides of the integral equations contain the incoming fields $\boldsymbol{E}^{\text{in}}$ and $\boldsymbol{H}^{\text{in}}$.

The integral kernels $G^A_{\alpha\beta}(\rho, z_\alpha, z'_\beta)$ and $G^V_{\alpha\beta}(\rho, z_\alpha, z'_\beta)$ in (9) and (10) are simple functions of the Sommerfeld vector ($\boldsymbol{A}$ and $\boldsymbol{F}$) and scalar (V_A and V_F) potentials of a horizontal electric and magnetic Hertzian dipole source in the layered medium [22], [23]. The superindices A and V denote the type of coupling (A = current and V = charge coupling). The subindices $\alpha, \beta = m, s$ denote the type of circuit level (m = microstrip, s = slotline) where the excitation and observation point are taken. For any fixed observation ($z = z_\alpha$) and excitation ($z = z'_\beta$) level in the layered medium, these integral kernels are scalar functions of the lateral distance ρ between the field and the source point. This property makes them very suitable for tabulation.

Starting from the Sommerfeld scalar and vector potentials, the resulting MPIE formulation (9), (10) for hybrid microstrip-slotline structures uses only two scalar functions for each excitation and observation level. An additional advantage is that the integral kernels for the reciprocal interactions are symmetrical, i.e. $G^A_{\alpha\beta}(\rho, z_\alpha, z'_\beta) = G^A_{\beta\alpha}(\rho, z_\beta, z'_\alpha)$ and $G^V_{\alpha\beta}(\rho, z_\alpha, z'_\beta) = G^V_{\beta\alpha}(\rho, z_\beta, z'_\alpha)$ for any $\alpha, \beta = m, s$. This follows from the Lorentz reciprocity theorem and allows for a further reduction of the number of Green's functions which need to be calculated and tabulated.

A mesh of rectangular and triangular cells is used to subdivide both the microstrip and the slotline structures. Uniform rectangular cells are used in the major part of the structure, allowing the possibility to take advantage of translational symmetry to speed up the calculations. The flexibility to model arbitrarily shaped junctions is preserved by using triangles in those parts of the structure which do not fit into a rectangular mesh. The classical vector valued rooftop expansion functions $\boldsymbol{b}_i(\boldsymbol{r}), i = 1, \cdots, M$ are used to model the electric and magnetic currents in the rectangular mesh, while triangular vector valued rooftop functions [1] are adopted in the triangular cells. The triangular rooftop function basically consists of a pair of linearily varying functions with triangular support. The current distribution within each cell is expressed in terms of its normal components on the sides of the cell. It has been shown in [10] that this combination allows us to mix rectangular and triangular cells in a self-consistent manner, i.e. the normal component of the current density is required to be continuous across the cell boundaries, avoiding the unphysical occurence of Dirac-function line charges at the junction of two adjacent cells. The analytical expressions of these rooftop functions are given in [10] and will not be repeated here.

The system matrix equation $\boldsymbol{Z} \cdot \boldsymbol{I} = \boldsymbol{V}$ follows from the testing of the integral equations with the same rooftop expansion functions (Galerkin testing). Although simpler test functions can be used, the Galerkin technique is preferred because it results in a symmetric $\boldsymbol{Z}$-matrix. This implies that reciprocity, which is a fundamental property of electromagnetic fields in a linear, isotropic medium, is preserved in the approximation process using Galerkin's technique. This also implies that only half of the $\boldsymbol{Z}$-matrix elements must be calculated and stored. This advantage is very important when electrically large structures are modelled, since the available amount of computer memory places an upper limit to the dimensionality of the $\boldsymbol{Z}$-matrix and thus the complexity of the structures which can be handled directly.

With Galerkin's technique, each element in $\boldsymbol{Z}$ represents the coupling or interaction between two expansion functions and is given by a quadruple spatial interaction integral. An efficient analytical calculation scheme for these quadruple integrals will be discussed in Section III. The right hand side vector $\boldsymbol{V}$ represents the excitation mechanism of the structure. The solution of the matrix equation yields the electric surface current distribution on the microstrip structures and the magnetic surface current distribution on the slotline structures.

In order to find the circuit parameters, calibration port transmission lines of finite length are added to the ports of the structure (Fig. 1). The planar circuit is excited by mathematical current sources located at the far ends of the calibration lines. The source current distribution is modelled with the same rooftop functions, but with impressed amplitude. This means that the calculation of the $\boldsymbol{V}$-matrix elements is essentialy the same as the calculation of the $\boldsymbol{Z}$-matrix elements. The circuit port voltage $V_{p,i}$ and current $I_{p,i}$ at port i follow from a 3D power-current (microstrip ports) or power-voltage (slotline ports) calculation, depending on the type of the corresponding port transmission line.

For a port i on a microstrip level, an electric current density $\boldsymbol{J}_{p,i}(\boldsymbol{r})$ is impressed at the far end of the corresponding port transmission line. The associated port current $I_{p,i}$ follows from the calculation of the flux of the impressed current density over the width of the port transmission line. The complex power $P_{p,i}$ launched into the system by the impressed current source $\boldsymbol{J}_{p,i}(\boldsymbol{r})$ can be calculated from the field solution by integrating the scalar product of the tangential electric field

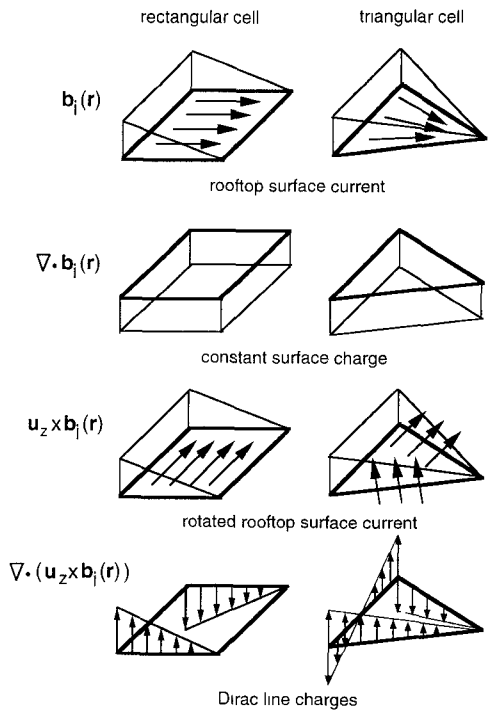

Fig. 2. Rectangular and triangular expansion functions modelling the current and charge contributions of hybrid microstrip-slotline interactions.

and the complex conjugate of the impressed port current. The voltage $V_{p,i}$ at the microstrip port is derived from this 3D power-current calculation

$$P_{p,i} = -\frac{1}{2}\iint_{S_{p,i}} \boldsymbol{E}(\boldsymbol{r}) \cdot \boldsymbol{J}^*_{p,i}(\boldsymbol{r})\, dS = \frac{1}{2} V_{p,i} I^*_{p,i}$$

$$I_{p,i} = \int_{L_{p,i}} \boldsymbol{J}_{p,i}(\boldsymbol{r}) \cdot d\boldsymbol{n}. \tag{11}$$

In (11), $S_{p,i}$ is the region over which the excitation current $\boldsymbol{J}_{p,i}(\boldsymbol{r})$ is defined and $\boldsymbol{E}(\boldsymbol{r})$ is the total electric field. $L_{p,i}$ is the integration path at the far end of the feedline and $\boldsymbol{n}$ is the unit vector normal to $L_{p,i}$.

For a port i lying on a slotline level, a magnetic current density $\boldsymbol{M}_{p,i}(\boldsymbol{r})$ or port voltage $V_{p,i}$ is impressed. The corresponding port current follows from a 3D power-voltage calculation

$$P_{p,i} = -\frac{1}{2}\iint_{S_{p,i}} \boldsymbol{H}^*(\boldsymbol{r}) \cdot \boldsymbol{M}_{p,i}(\boldsymbol{r})\, dS = \frac{1}{2} V_{p,i} I^*_{p,i}$$

$$V_{p,i} = \int_{L_{p,i}} \boldsymbol{M}_{p,i}(\boldsymbol{r}) \cdot d\boldsymbol{n} = \int_{L_{p,i}} \boldsymbol{E}(\boldsymbol{r}) \cdot d\boldsymbol{t}. \tag{12}$$

The complete description of the circuit requires the simulation of a number of independent excitation states equal to the number of ports. The influence of the port transmission lines and the port current sources are removed using an equivalent circuit calibration technique. In this approach, each uncoupled port transmission line is modelled as a general two-port, linear, reciprocal network and characterized by the simulation of a perfect through standard. This information is then used to remove the port tranmission lines from the simulation results of the N-port circuit. This calibration technique has the advantage over the more traditional VSWR methods [6] that no reference is made to a current standing wave pattern on the feed lines, allowing one to choose shorter feedlines.

III. Calculation of the Quadruple Interaction Integrals

In this section, an analytical calculation scheme for the quadruple interaction integrals is described. The elements of the interaction matrix $\boldsymbol{Z}$ determine the coupling between two expansion functions and follow from the integral equations (9) and (10). Using elementary calculus, the hybrid microstrip-slotline cell-cell interactions can be transformed into the following general form:

$$Z_{ij} = \iint_{K_i} dS \iint_{K_j} dS' \left[G^A_{\alpha\beta}(\boldsymbol{r}, \boldsymbol{r}') \boldsymbol{J}_i(\boldsymbol{r}) \cdot \boldsymbol{J}_j(\boldsymbol{r}') + G^V_{\alpha\beta}(\boldsymbol{r}, \boldsymbol{r}') \nabla \cdot \boldsymbol{J}_i(\boldsymbol{r}) \nabla' \cdot \boldsymbol{J}_j(\boldsymbol{r}') \right]$$

with

$$\boldsymbol{J}_i(\boldsymbol{r}) = \begin{cases} \boldsymbol{b}_i(\boldsymbol{r}); & \text{for } K_i \in \text{strip } (\alpha\beta = mm, ms) \\ & \quad \text{or } K_i \in \text{slot } (\alpha\beta = ss) \\ \boldsymbol{u}_z \times \boldsymbol{b}_i(\boldsymbol{r}); & \text{for } K_i \in \text{slot } (\alpha\beta = sm) \end{cases}$$

$$\boldsymbol{J}_j(\boldsymbol{r}) = \begin{cases} \boldsymbol{b}_j(\boldsymbol{r}); & \text{for } K_j \in \text{strip } (\alpha\beta = mm, sm) \\ & \quad \text{or } K_j \in \text{slot } (\alpha\beta = ss) \\ \boldsymbol{u}_z \times \boldsymbol{b}_j(\boldsymbol{r}); & \text{for } K_j \in \text{slot } (\alpha\beta = ms). \end{cases} \tag{13}$$

In (13) $\boldsymbol{r}$ and $\boldsymbol{r}'$ are position vectors in K_i and K_j, the domains of $\boldsymbol{J}_i(\boldsymbol{r})$ and $\boldsymbol{J}_j(\boldsymbol{r}')$. The well known vector-valued rooftop functions $\boldsymbol{b}_i(\boldsymbol{r})$ are used as test and expansion functions on the microstrip and slotline levels. For the microstrip-slotline interactions, the orientation of these rooftop functions is rotated over 90 degrees on the slotline levels as a consequence of the rotation of the magnetic current in (9) and the magnetic field in (10). The charge functions $\nabla \cdot \boldsymbol{b}_i(\boldsymbol{r})$ corresponding with the classical rooftop functions are constant over the corresponding cell. The charge functions $\nabla \cdot (u_z \times \boldsymbol{b}_i(\boldsymbol{r}))$ corresponding with the rotated rooftop functions however are lineary varying Dirac line charges over the boundary of the corresponding cell. This implies that for the microstrip-slotline interaction, the surface integral in (13) is reduced to a line integral. Fig. 2 illustrates the impact of the rotation on the corresponding charge functions for a rectangular and a triangular cell.

The spatial Green's functions in (13) follow from an inverse Hankel transformation of the spectral Green's functions. The latter result from the solution of the spectral TE_z and a TM_z transmision line cascade associated with the layered medium in which the planar structure is embedded. We refer to [22] and [23] for more details on these calculations. In order to calculate Z_{ij}, the integral kernels G^A and G^V are precalculated and curve-fitted into a local power series of the lateral distance over the range of ρ determined by the minimum and maximum distance between the two cells K_i and K_j

$$G^{V,A}(\boldsymbol{r}, \boldsymbol{r}') = \sum_{p=0}^{\max p} g_p^{V,A} (\rho - \rho_g)^p \tag{14}$$

where $g_p^{V,A}$ are the curve-fitting coefficients and ρ_g is the distance between the centers of gravity of the two cells. The number of power terms in (14) depends on the lateral separation of the excitation and the observation cell and the error that is allowed for the cell-cell coupling. For the self-patch and nearby interactions, the $1/\rho$ singularity in the Green's functions is taken into account explicitly.

Since the rooftop functions $\boldsymbol{b}_i(\boldsymbol{r})$ are linear functions in (x, y) and the integral kernels are curve-fitted into polynomials, the basic double surface integrals involved in (13) are simplified and written in matrix notation as

$$\boldsymbol{Q}_P(K_i, K_j, p) = \iint_{K_i} dS \iint_{K_j} dS' \begin{bmatrix} 1 \\ x \\ y \end{bmatrix} [1 \quad x' \quad y'] \cdot (\rho - \rho_g)^p; \qquad p = 0, \cdots, \max p \tag{15}$$

where $\boldsymbol{Q}_P$ is a 3×3 matrix of quadruple integrals. Matrix notation is adopted here for mathematical convenience. The quadruple integrals in (15) can be solved fully analytically for K_i and K_j of general polygonal shape. In the analytical treatment a distinction is made between close and distant coupling.

For close coupling, the integration over the excitation cell K_j is performed analytically in the polar coordinates (ρ, θ) determined by the lateral separation between the excitation and the observation point, i.e. $\boldsymbol{r}_t - \boldsymbol{r}'_t = \rho(\cos\theta \boldsymbol{u}_x + \sin\theta \boldsymbol{u}_y)$. The integration domain K_j (which can be of general polygonal shape) is divided into a finite number of triangles $K_j^{(m)}$, as depicted in Fig. 3. All triangles $K_j^{(m)}$ have in the observation point $\boldsymbol{r}$ one vertex in common. The result of the integration over the triangle $K_j^{(m)}$ is written as the difference of two "point"-contributions associated with the two cell vertex points $P_{j,1}$ and $P_{j,2}$

$$\boldsymbol{Q}_P(K_i, K_j, p) = \sum_m [\boldsymbol{Q}_P^{(m)}(K_i, P_{j,2}^{(m)}, p) - \boldsymbol{Q}_P^{(m)}(K_i, P_{j,1}^{(m)}, p)]. \tag{16}$$

Each point-contribution still contains the integration over the observation cell K_i. After translation and rotation of the (x, y) coordinate system to the local coordinate system $(X^{(m)}, Y^{(m)})$ associated with each vertex point $P_j^{(m)}$ of side (m) (see Fig. 3), the point-contributions are reduced to a combination of two types of surface integrals. We have

$$\boldsymbol{Q}_P^{(m)}(K_i, P_j^{(m)}, p) = \sum_{\substack{k,l=0,1,2 \\ k+l\le 2}} \boldsymbol{M}_{P,0}(P_j^{(m)}, k, l, p) B_{P,0}(K_i, k, l, p) + \sum_{\substack{k=1,2 \\ l=0,1 \\ k+l\le 2}} \boldsymbol{M}_{P,2}(P_j^{(m)}, k, l) B_{P,2}(K_i, k, l, p). \tag{17}$$

The explicit expressions of the $\boldsymbol{M}_{P,0}$ and $\boldsymbol{M}_{P,2}$ coefficient matrices in (17) follow from the coordinate transformation by which the (x, y) coordinate system is replaced by the $(X^{(m)}, Y^{(m)})$ coordinate system. Their derivation is straightforward and is therefore omitted here. The surface integrals $B_{P,0}$ and $B_{P,2}$ in (17) are given by a recurrence relation as a combination of three basis type integrals

$$\begin{aligned} B_{P,0}(K_i, k, l, -1) &= B_3(K_i, k+1, l) \\ B_{P,0}(K_i, k, l, 0) &= \frac{1}{2} B_1(K_1, k+1, l+1) \\ B_{P,0}(K_i, k, l, p) &= \frac{1}{(p+1)(p+2)} [B_2(K_i, k+1, l+1, p) \\ &\quad + p^2 B_{P,0}(K_i, k+2, l, p-2)] \end{aligned} \tag{18}$$

and

$$\begin{aligned} B_{P,2}(K_i, k, l, -1) &= -\frac{1}{2} B_2(K_i, k, l, 1) \\ B_{P,2}(K_i, k, l, 0) &= -\frac{1}{6} [B_1(K_i, k+2, l) \\ &\quad + B_1(K_i, k, l+2)] \\ B_{P,2}(K_i, k, l, p) &= \frac{p(p+1)}{(p+2)(p+3)} \\ &\quad \cdot [B_{P,2}(K_i, k+2, l, p-2) \\ &\quad + B_{P,2}(K_i, k, l+2, p-2)]. \end{aligned} \tag{19}$$

The basis surface integrals involved in (18) and (19) are of the following form:

$$\begin{aligned} B_1(K_i, k, l) &= \iint_{K_i} dS x^k y^l; \qquad k, l = 0, 1, 2, \cdots \\ B_2(K_i, k, l, m) &= \iint_{K_i} dS x^k y^l (\sqrt{x^2 + y^2})^m; \\ &\qquad k, l = 0, 1, 2, \cdots, \quad m = 1, 2, \cdots \\ B_3(K_i, k, l) &= \iint_{K_i} dS x^k y^l \ln(y + \sqrt{x^2 + y^2}); \\ &\qquad k, l = 0, 1, 2, \cdots. \end{aligned} \tag{20}$$

The analytical evaluation of these surface integrals is possible for any value of the indices k, l and m, making extensive use of recurrence relations. The mathematics are very elaborate but straightforward and will not be included here. The approach described in this section has the advantage that recurrence relations are obtained for the $B_{p,0}$ and $B_{p,2}$ integrals which express the higher order power terms of ρ in terms of the two lowest order ones, i.e. higher order terms are calculated at very low computational cost. The use of such a recurrence relation allows a very efficient implementation of the algorithm and reduces the CPU-time needed for these calculations significantly.

For distant coupling, the power term $(\rho - \rho_g)^p$ is expanded into a Taylor series around the distance between the centers of gravity of the two cells

$$(\rho - \rho_g)^p = \sum_{N=0}^{\text{Order}} \sum_{\substack{0\le k,l,m,n\le N \\ k+l+m+n=N}} C_{k,l,m,n}(p)(x - x_g)^k \cdot (y - y_g)^l (x' - x'_g)^m (y' - y'_g)^n \tag{21}$$

where (x_g, y_g) is the center of gravity of the cell S_i and (x'_g, y'_g) is the center of gravity of the cell S_j. The expansion order in (21) depends on the distance between the two cells and

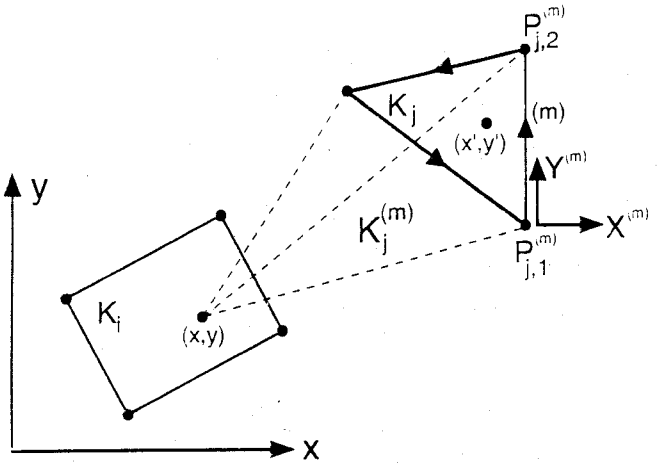

Fig. 3. General picture of an observation cell K_i and an excitation cell K_j. The excitation cell is divided into a finite number of triangles $K_j^{(m)}$.

TABLE I
MESH PARAMETERS USED IN THE SIMULATION

	mesh parameters		cell sizes (microstrip)		cell sizes (slotline)		total number
	N_x	N_y	D_x (mm)	D_y(mm)	D_x (mm)	D_y(mm)	of cells
mesh 1	1	20	2.00	2.54	1.10	1.875	38
mesh 2	2	40	1.00	1.27	0.55	1.00	150
mesh 3	3	60	0.75	0.8467	0.3667	0.635	312
mesh 4	4	80	0.50	0.635	0.275	0.50	600

the desired accuracy. The Taylor series expansion coefficients in (21) are calculated as Nth order partial derivatives of the power term $(\rho - \rho_g)^p$

$$C_{k,l,m,n}(p) = \frac{1}{k!l!m!n!} \frac{\delta^N}{\delta x^k \delta y^l \delta x'^m \delta y'^n} \cdot ((\rho - \rho_g)^p) \Big|_{\substack{x = x_g \\ y = y_g \\ x' = x'_g \\ y' = y'_g.}} \tag{22}$$

Their calculation is straightforward for any value of p. Substituting (21) into (15), the quadruple integrals fall apart into the product of two simple surface integrals of the type B_1. Distant cell-cell coupling terms are typically calculated a factor 30 faster than selfpatch coupling terms. This new scheme for the distant cell-cell coupling elements further reduces the CPU-time. It also eliminates the numerical noise which occurs in the exact analytical solution technique of (15) for large cell-cell separations, due to the round-off errors from the numerical subtraction of two large, almost equal contributions.

IV. NUMERICAL RESULTS

A general computer program has been written to calculate the S-parameters of multilayered hybrid microstrip-slotline planar circuits. The MPIE is solved using rectangular and triangular rooftop expansion functions. The stability and the numerical convergence of this type of expansion functions has already been adressed in several other papers [6], [10], [25].

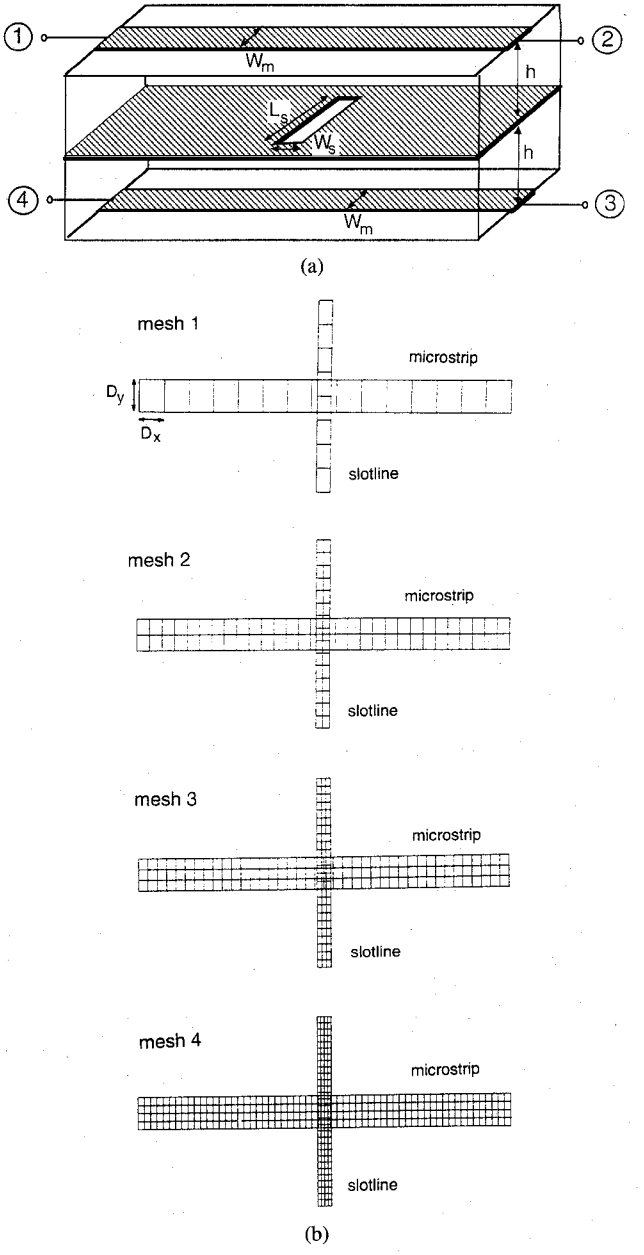

Fig. 4. (a) Geometry of the four-port aperture-coupled microstrip lines. ($W_m = 2.54$ mm, $W_s = 1.1$ mm, $L_s = 15$ mm, $h = 0.762$ mm, $\varepsilon_r = 2.22$.) (b) Top view of the meshes used in the simulations.

The numerical examples in this paper focus on the versatility of the computer program to model general polygonal shaped microstrip-slotline structures using a mixed mesh of rectangular and triangular cells. The simulation results for the structure in the first example are included for validation purposes, since we have found theoretical and measurement results in the literature to compare with.

A. Aperture-Coupled Microstrip Lines

The first example shows the simulation results for two parallel microstrip lines coupled by a small rectangular slot in a common ground plane. The geometry of this hybrid microstrip-slotline circuit is depicted in Fig. 4(a). The microstrip lines of width $W_m = 0.254$ mm are printed on a double layered di-

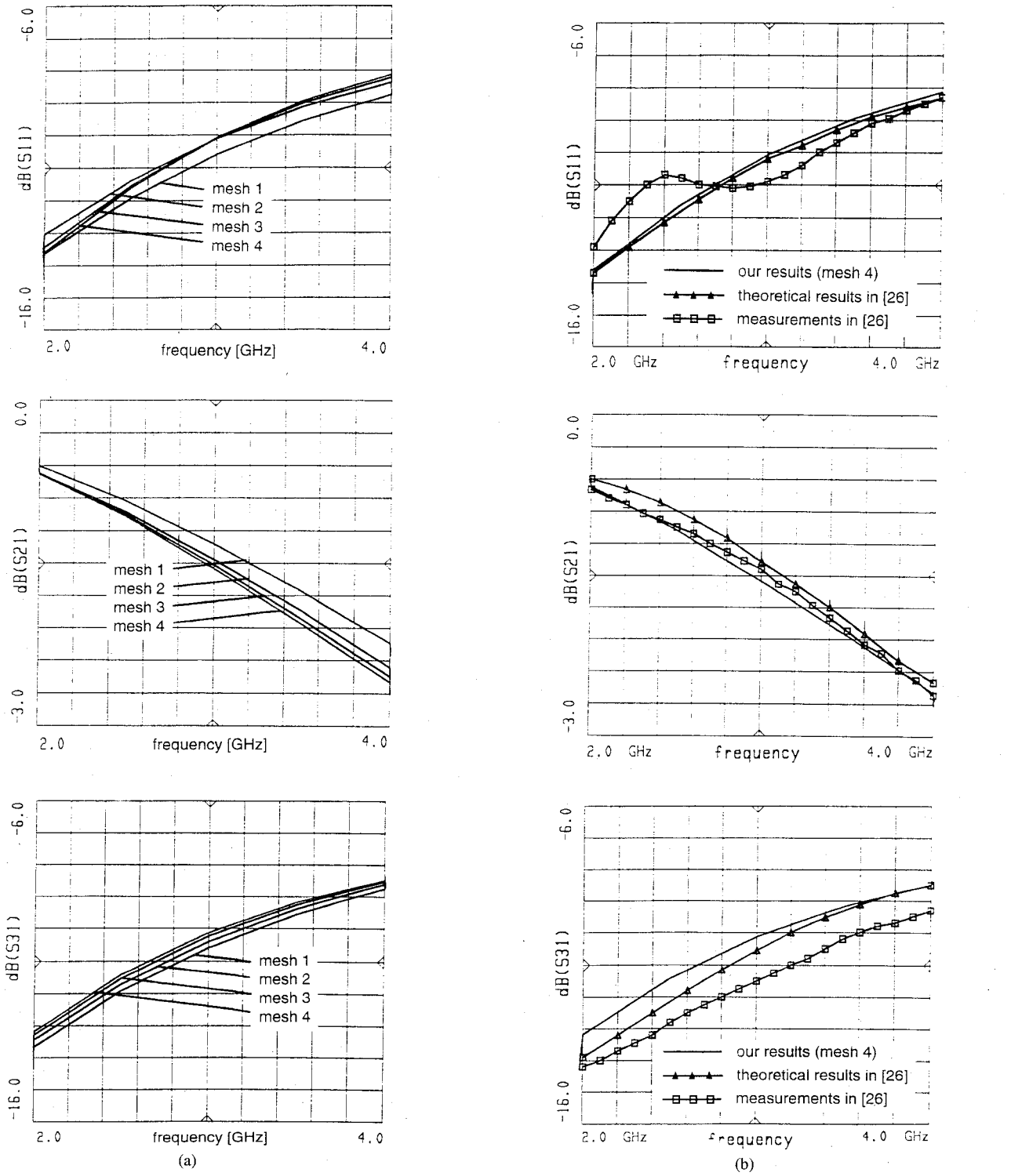

Fig. 5. Frequency characteristics of the aperture-coupled microstrip lines. (a) Results with the different meshes. (b) Comparison with the theoretical and measured data in [26].

electric substrate ($h = 0.762$ mm, $\varepsilon_r = 2.22$). The rectangular slot aperture is rotated over 90 degrees with respect to the propagation direction of the microstrip lines. The dimensions of the slot aperture are $L_s = 15$ mm and $W_s = 1.1$ mm. This structure has been analysed by Herscovici and Pozar in [26] and by Wakabayashi and Itoh in [27]. The planar circuit of Fig. 4(a) is modelled as a four-port network. In operation, an input signal applied to port 1 of the top microstrip line is partially coupled to the other microstrip line. This coupled power is equally divided between the ports 3 and 4 with a 180° phase shift. This property of the circuit finds application in the design of balanced mixer circuits and planar antenna feed networks.

The hybrid microstrip-slotline structure of Fig. 4(a) is simulated using a mixed mesh of rectangular cells with different cell dimensions in the microstrip and slotline transmission lines.

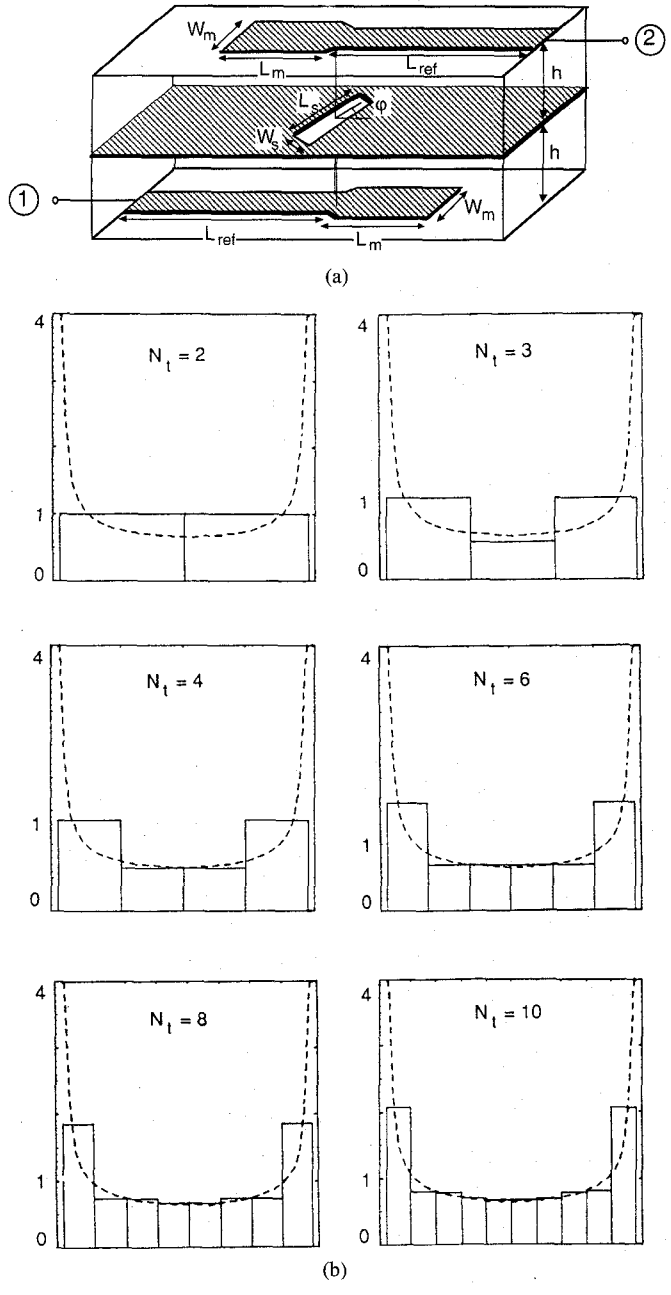

Fig. 6. (a) Geometry of the two-port aperture-coupled microstrip line transition. (b) Cross-sectional view of the current profile on the microstrip lines.

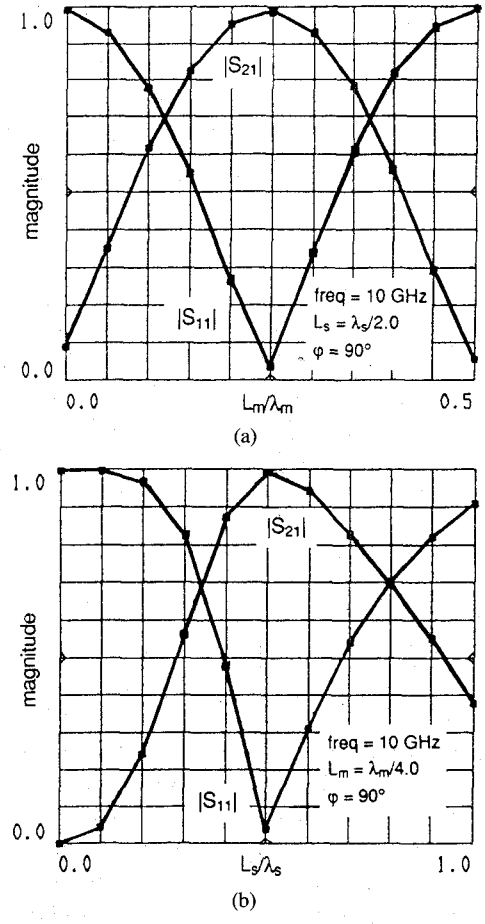

Fig. 7. (a) Variation of $|S_{11}|$ and $|S_{21}|$ with the microstrip stub electrical length. (b) Variation of $|S_{11}|$ and $|S_{21}|$ with the slotline aperture electrical length.

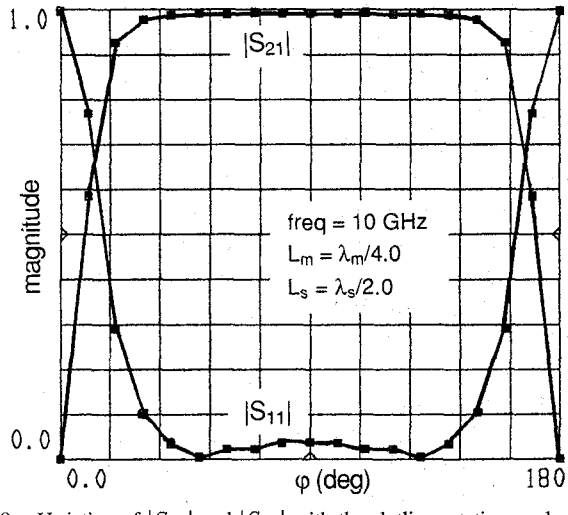

Fig. 8. Variation of $|S_{11}|$ and $|S_{21}|$ with the slotline rotation angle.

During the simulation, the frequency was swept between 2 GHz and 4 GHz. In order to estimate the error introduced by the discretization of the structures, the simulation was repeated using four different meshes with increasing cell density. The mesh parameters which were used are listed in Table I. The top view of these meshes is shown in Fig. 4(b). The mesh parameters are the number of cells (N_t) in the transverse direction of the transmission lines and the number of cells per wavelength (N_l) in the longitudinal direction of the transmission lines.

The calculated S_{11}, S_{21} and S_{31} parameters are plotted in Fig. 5(a) as a function of the frequency. It follows that the theoretical results only show a small shift with increasing cell density. The numerical results with the coarsest mesh are already within 1 dB accurate over the considered frequency range. In Fig. 5(b), we have verified our theoretical results by comparing them with the theoretical and the measured data published by Herscovici and Pozar in [26]. The ripples appearing in the measured data for the S_{21} and S_{31} parameters

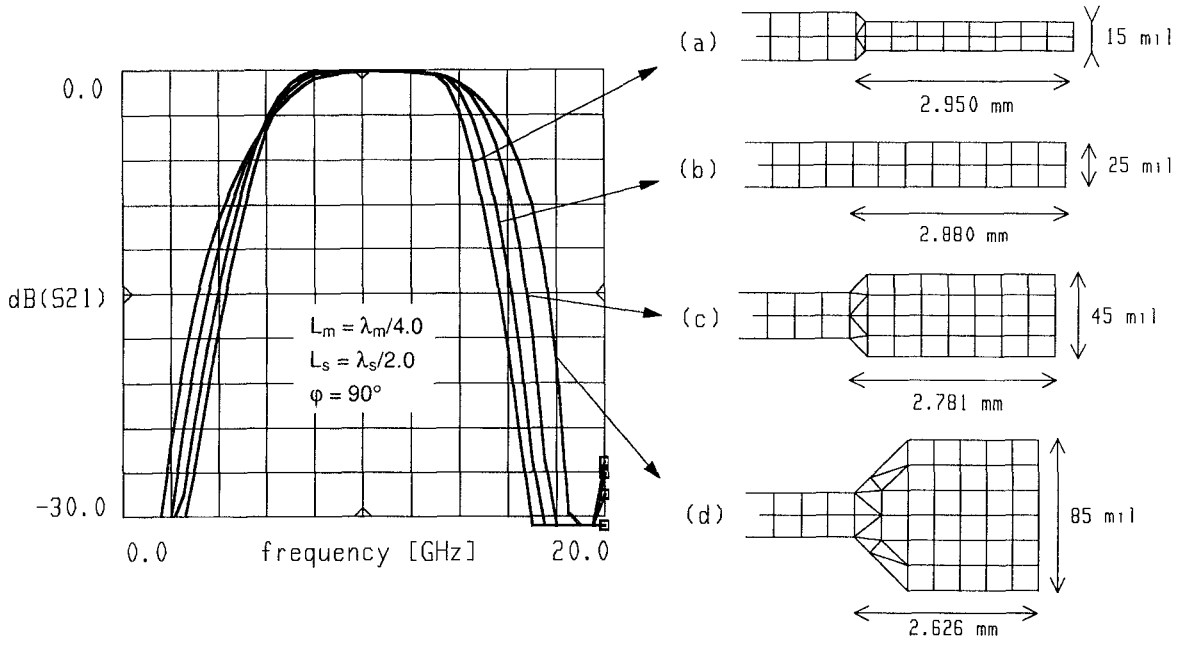

Fig. 9. Frequency characteristics of the two-port aperture-coupled microstrip line transition.

in [26] have a maximum amplitude of the order of 1 dB. These ripples are attributed to the imperfect contact of the two ground planes (the two substrates of the test structure in [26] were fabricated with two separate ground planes) and have been averaged out in Fig. 5(b). It follows from the plots in Fig. 5(b) that the theoretical results agree within 1 dB with the averaged experimental results.

B. Design of an X-Band Aperture-Coupled Microstrip Line Transition

By terminating two of the microstrip lines with stubs, the four-port network discribed in Section IV-A is reduced to a two-port aperture-coupled microstrip line transition circuit (Fig. 6(a)). This type of coupling circuit has been investigated by Schüppert in [28] and by Van den Berg and Katehi in [29]. By proper choise of the various geometrical parameters of the structure, the circuit can be designed to couple nearly all of the input power to the output port within a certain frequency band. This kind of circuit finds its application as a non-contacting interconnection between multilayered integrated circuits.

In this section, we will discuss the design of a symmetrical, slot-coupled, microstrip line transition with a maximally flat, 50-Ohm matched transmission characteristic in the X-band (8–12 GHz). The transition connects two microstrip tranmission lines, printed on each side of a double layered standard alumina substrate ($h = 25$ mil, $\varepsilon_r = 9.7$) by electromagnetic coupling through an aperture in the common ground plane. This structure is depicted in Fig. 6. The width of the transmission lines is 25 mil, corresponding to a 50-Ohms impedance level. The design parameters are the width W_m and the length L_m of the microstrip stubs, the width W_s and the length L_s of the slotline aperture and the rotation angle φ of the slotline with respect to the microstrip lines. The use of a mixed rectangular-triangular mesh in the simulation process, preserves the flexibility to change the geometrical design parameters with respect to each other, without restrictions. In the following discussion, the longitudinal mesh density is always choosen so that the longitudinal dimensions of the cells do not exceed $\lambda_g/30$, where λ_g is the guided wavelength at the considered frequency. This implies that the longitudinal mesh parameter is always greater than $N_l > 30$.

The initial width of the slotline aperture is choosen to be $W_s = 5$ mil, corresponding to a matched slotline ($Z_{0,s} = 50$ Ohms) at the X-band central frequency (10 GHz). The initial width of the microstrip stubs is choosen to be equal to the microstrip line width, i.e. $W_m = 25$ mil. A cross-sectional view of the current distribution on the microstrip lines at 10 Ghz, is shown in Fig. 6(b) for different number of cells in the transverse direction ($N_t = 2, 3, 4, 6, 8, 10$). The dashed line in the plots is the reference result obtained with a 2D cross-section solver [30]. The singular edge behavior of the current is better approximated as N_t increases. However, the numerical results of the convergence study in the first example showed that a mesh density with $N_t = 2$ already gives sufficient accurate S-parameters. In the following, the transverse mesh parameter in the transmission lines is fixed at $N_t = 2$.

Fig. 7(a) and (b) illustrate the effect of the electrical length of the microstrip stubs L_m/λ_m and the electrical length of the slotline aperture L_s/λ_s on the transmission and reflection coefficients. λ_m and λ_s are the guided wavelengths on the microstrip and the slotline tranmission lines. The plots in Fig. 7 were computed at the X-band central frequency. As can be seen in Fig. 7(a), varying the electrical length of the microstrip stubs has the effect of changing the position of the current maxima on the microstrip lines and thus varying the degree of coupling through the slot. This coupling is maximal

for a stub length of $L_m = \lambda_m/4.0$ at which the open at the end of the stub is transformed to a virtual short just under the slotline aperture. The same conclusion follows from varying the electrical length of the slotline aperture (Fig. 7(b)). Here, the coupling is maximal for a slotline length of $L_s = \lambda_s/2.0$ at which the shorts at the ends of the aperture are transformed to a virtual open or a magnetic current maxima just above the microstrip lines. Fig. 7(b) also demonstrates that as the slotline length increases in multiples of λ_s, the slotline aperture is virtually short circuited and coupling is reduced.

Fig. 8 illustrates the effect of the rotation angle φ of the slotline, for optimally choosen microstrip stub and slotline lengths ($L_m = \lambda_m/4.0$ and $L_s = \lambda_s/2.0$). It follows that varying the rotation angle has very little effect on the coupling performance in the range $45° < \varphi < 135°$. However, the coupling performance is affected very strongly outside this range and is totally reduced when the slotline aperture and the microstrip lines are parallel ($\varphi = 0°$ or $\varphi = 180°$).

Finally, the frequency characteristic of the S_{21}-parameter is plotted in Fig. 9 for different widths of the microstrip stub ($W_m = 15$, 25, 45, 85 mil). The connection with the microstrip feedline is provided by a small tapered section of 45°. The other geometrical parameters are choosen such that an optimal coupler performance is obtained at 10 GHz ($L_m = \lambda_m/4, W_s = 5$ mil, $L_s = \lambda_s/2$ and $\varphi = 90°$). Also shown in Fig. 9 is a detail of the mixed rectangular-triangular mesh, which has been used to simulate the tapered microstrip section for different widths of the microstrip stub. The plots in Fig. 9 show that the coupler performance is very good in the frequency range from 6–14 GHz and decreases very fast outside this frequency range. The plots also indicate that the 3-dB bandwidth of the coupler increases slightly with increasing microstrip stub width.

V. Conclusion

We have presented a mixed potential integral equation technique for the simulation of arbitrarily shaped hybrid microstrip-slotline structures embedded in a multilayered medium. The method of moments in combination with Galerkin's technique is applied to the solution of the mixed potential integral equation in the spatial domain. A mixed mesh consisting of different rectangular and triangular cells is used to subdivide the structure. Rooftop expansion functions are used to model the electric currents on the microstrip structures and the magnetic currents in the slotline apertures. The introduction of equivalent magnetic currents in the slotline structures reduces the meshing of the infinite metallization patterns at the slotline levels to the meshing of the finite slotline apertures. A efficient calculation technique is used to calculate the quadruple interaction integrals. Two examples of hybrid microstrip-slotline circuits have been discussed. In the first example, the simulation results for a microstrip-slotline transition are compared with theoretical and measured data from the literature. The second example illustrates the use of the simulation technique in the design proces of a broadband slot-coupled microstrip line transition.

Acknowledgment

The authors would like to thank K. Blomme, J. Van Hese, and L. Van Dormael for the development of the Green's functions without which it would have been impossible to obtain the results presented in this paper. The authors would also like to thank the reviewers for there valuable suggestions.

References

[1] S. M. Rao, D. R. Wilton, and A. Glisson, "Electromagnetic scattering by surfaces of arbitrary shape," *IEEE Trans. Antenn. Propagat.*, vol. AP-30, pp. 409–418, May 1982.
[2] J. C. Rautio and R. F. Harrington, "An electromagnetic time-harmonic analysis of shielded microstrip circuits," *IEEE Trans. Microwave Theory Tech.*, vol. MTT-35, pp. 726–730, Aug. 1987.
[3] J. R. Mosig, "Arbitrarily shaped microstrip structures and their analysis with a mixed potential integral equation," *IEEE Trans. Microwave Theory Tech.*, vol. MTT-36, pp. 314–323, Feb. 1988.
[4] R. W. Jackson, "Full-wave, finite element analysis of irregular microstrip discontinuities," *IEEE Trans. Microwave Theory Tech.*, vol. MTT-37, pp. 81–89, Jan. 1989.
[5] W. P. Harokopus Jr. and P. B. Katehi, "Characterization of microstrip discontinuities on multilayer dielectric substrates including radiation losses," *IEEE Trans. Microwave Theory Tech.*, vol. MTT-37, pp. 2058–2066, Dec. 1989.
[6] W. Wertgen and R. H. Jansen, "Efficient direct and iterative electrodynamic analysis of geometrically complex MIC and MMIC structures," *Int. J. Numerical Modelling: Electronic Networks, Devices and Fields*, vol. 2, pp. 153–186, 1989.
[7] S. C. Wu, H. Y. Yang, N. G. Alexopoulos, and I. Wolff, "A rigorous dispersive characterization of microstrip cross and T junctions," *IEEE Trans. Microwave Theory Tech.*, vol. MTT-38, pp. 1837–1843, Dec. 1990.
[8] A. Hill and V. K. Tripathi, "An efficient algorithm for the three-dimensional analysis of passive microstrip components and discontinuities for microwave and millimeter-wave integrated circuits," *IEEE Trans. Microwave Theory Tech.*, vol. MTT-39, pp. 83–91, Jan. 1991.
[9] N. I. Dib, L. P. B. Katehi, G. E. Ponchak, and R. N. Simons, "Coplanar waveguide discontinuities for p-i-n diode switches and filter applications," in *IEEE MTT-S Dig.*, 1990, pp. 399–402.
[10] D. C. Chang and J. X. Zheng, "Electromagnetic modeling of passive circuit elements in MMIC," *IEEE Trans. Microwave Theory Tech.*, vol. MTT-40, pp. 1741–1747, Sept. 1992.
[11] T. S. Horng, W. E. McKinzie, and N. G. Aloxopoulos, "Full-wave spectral-domain analysis of compensation of microstrip discontinuities using triangular subdomain functions," *IEEE Trans. Microwave Theory Tech.*, vol. MTT-40, pp. 2137–2147, Dec. 1992.
[12] J. Sercu, N. Faché, F. Libbrecht, and D. De Zutter, "Study of gridding and cell-cell interactions in the method of moments analysis of arbitrarily shaped planar circuits," in *IEEE MTT-Symp. Dig.*, 1993, pp. 753–756.
[13] J. Sercu, H. Devos, N. Faché, and D. De Zutter, "Efficient calculation technique for the impedance matrix equation in the MPIE technique for microstrip and slotline planar structures of arbitrary shape," in *IEEE APS-Symp. Dig.*, 1993, pp. 350–353.
[14] J. Sercu, N. Faché, F. Libbrecht, and D. De Zutter, "Full-wave space-domain analysis of open microstrip discontinuities including the singular current-edge behavior," *IEEE Trans. Microwave Theory Tech.*, vol. MTT-41, pp. 1581–1588, Sept. 1993.
[15] H. Yang and N. G. Alexopoulos, "A dynamic model for microstrip-slotline transition and related structures," *IEEE Trans. Microwave Theory Tech.*, vol. MTT-36, no. 2, pp. 286–293, Feb. 1988.
[16] T. Itoh, *Numerical Techniques for Microwave and Millimeter-Wave Passive Structures.* Wiley, 1989.
[17] HP-Momentum, Hewlett-Packard, Palo Alto, CA.
[18] EMSI, EEsof, Westlake Village, CA.
[19] Explorer, Compact Software, Paterson, NJ.
[20] em, Sonnet Software, Liverpool, NY.
[21] SFPMIC+, Jansen Microwave, Ratingen, Germany.
[22] N. Faché, J. Van Hese, and D. De Zutter, "Generalized space domain Green's dyadic for multilayered media with special application to microwave interconnections," *JEWA*, vol. 3, no. 7, pp. 651–669, 1992.
[23] K. Blomme, N. Faché, and D. De Zutter, "A general calculation technique for the Green's functions in the mixed potential integral equation formulation of microstrip-slot circuits," in *IEEE APS-93 Symp. Dig*, 1993, pp. 650–653.

[24] J. Sercu, N. Faché, and D. De Zutter, "Characterization of TEM and non-TEM planar transmission lines with a full wave 3D field analysis technique," in *Proc. 23th European Microwave Conf.*, 1993, pp. 328–329.
[25] J. Sercu, N. Faché, and P. Lagasse, "First-order rooftop functions for the current discretization in the method of moments solution of planar structures," in *IEEE Antenn. Propagat. Symp. Dig.*, 1994, Washington, D.C.
[26] N. Herscovici and D. M. Pozar, "Full-wave analysis of aperture-coupled microstrip lines," *IEEE Trans. Microwave Theory Tech.*, vol. MTT-39, pp. 1108–1114, July 1991.
[27] T. Wakabayashi and T. Itoh, "Three-dimensionally coupled microstrip lines via a rotated slot in a common ground plane," in *IEEE MTT-S Dig.*, 1992, pp. 999–1002.
[28] B. Schüppert, "Microstrip/slotline transitions: Modelling and experimental investigation," *IEEE Trans. Microwave Theory Tech.*, vol. MTT-36, pp. 1272–1282, Aug. 1988.
[29] N. L. Van den Berg and P. B. Katehi, "Full-wave analysis of aperture coupled shielded microstrip lines," in *IEEE MTT-S Dig.*, 1990, pp. 163–166.
[30] G. Coen, "Spectral domain analysis of microstrip structures," thesis, Univ. of Ghent, 1992.

Jeannick Sercu (S'89) was born in Ieper, Belgium, on February 9, 1967. He received the degree in electrical engineering from the University of Ghent in June 1990. In June 1994, he obtained the Ph.D. degree in electrical engineering at the same University for his research on the full-wave simulation of planar structures embedded in multilayered media. This work was sponsored by the National Fund for Scientific Research in Belgium.

Currently, he works as a research assistant at the Department of Information Technology (INTEC) of the University of Ghent. His research now focusses on efficient calculation techniques for electromagnetic field simulations of microwave and RF multilayered planar circuits.

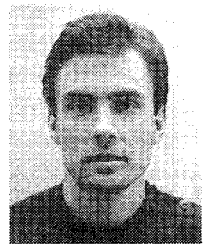

Niels Faché (S'92–M'92–M'92) was born July 4, 1964 in Ghent, Belgium. He received the degree in electrical engineering at the Ph.D. degree from the University of Ghent, Ghent, Belgium, in 1986 and 1989, respectively.

In 1990, he worked as a consultant from the Laboratory of Electromagnetism and Acoustics (LEA), University of Ghent to the Network Measurement Division of Hewlett-Packard, Santa Rosa, CA, where he worked on the improvement and implementation of linear models in the Microwave Design System. From 1991–1992 he was back at LEA, where he was engaged in the research on electromagnetic field solvers and their use in circuit simulators. In November 1992 he co-founded Alphabit, a Belgian CAE software company. He is currently Director of Alphabit. The company's activities focus on the development of electromagnetic field solvers for the simulation of high frequency circuits. He has made contributions to more than 30 papers in international journals and conference proceedings. He is also the principal author of the book, *Electromagnetic and Circuit Modelling of Multiconductor Transmission Lines* (Oxford University Press, 1992).

Frank Libbrecht was born in Kortrijk, Belgium, on September 22, 1964. He received the degree in electrical engineering from the University of Ghent in July, 1987. He received the Ph.D. degree from the same University in 1991 for his research on optical transmission of information.

His research now focuses on electromagnetic simulation of microwave planar structures.

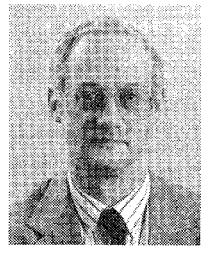

Paul Lagasse (M'83–SM'91) received the degree in electrical engineering in 1969 and the Ph.D. degree in 1972, both from the University of Ghent, Belgium.

In 1981 he became professor of electrical engineering at the University of Ghent, where he is now Head of the Department of Information Technology. Having originally worked in the area of surface acoustic waves, he is now mainly active in the fields of optoelectronics, high frequency technology, and integrated broadband telecommunications.